Tenth International Conference on Computational Fluid Dynamics (ICCFD10), Barcelona, Spain, July 9-13, 2018

ICCFD10-2018 10-114

Solving three dimensional turbulent compressible flows using a high order One Step Monotony Preserving scheme

I. Ben Hassan Saïdi*, C. Tenaud* and G. Fournier**
Corresponding author: iben@limsi.fr

* LIMSI, CNRS, Univ. Paris-Sud, Université Paris-Saclay, Orsay, FRANCE.
** LMEE, Université d'Évry-Val-d'Essonne, Université Paris-Saclay, Évry, FRANCE.

Abstract: A high order One Step Monotony Preserving scheme has been developed to compute the convective fluxes of the compressible Navier Stokes equations. This finite-volume solver, based on the Lax-Wendroff approach, is 7^{th} order both in space and time. A Monotony Preserving criteria is used to compute the discontinuities with accuracy, without spoiling the solution. Centered approximations are used to compute the diffusive fluxes of the Navier Stokes equations. In this article, we evaluate separately the ability of the solver to compute turbulent and shocked flows by simulating two test cases. The first test case is the 3 dimensional Taylor-Green vortex that allows to simulate a turbulent energy cascade in the framework of isotropic homogeneous turbulence. It is used to evaluate the accuracy of the solver to compute continuous turbulent solutions. The second test case is the steady shock-wave laminar boundary layer interaction. It is used to evaluate the shock capturing procedure of the solver.

Keywords: High-order Finite-Volume scheme, Monotony-Preserving criteria, Taylor-Green vortex, Shock-Wave boundary layer interaction.

1 Introduction

Direct Numerical Simulation (DNS) of high Reynolds number compressible flows involving shock waves is a challenging task since one must use a numerical scheme that can both represent small scale structures with the minimum of numerical dissipation, and capture discontinuities with the robustness that is common to Godunov-type methods without spoiling the accuracy in the vicinity of the discontinuity. In this context, a high order One-Step Monotonicity-Preserving (OSMP) scheme [1] has been developed by following a Lax-Wendroff approach. For discontinuity capturing, Monotonicity-Preserving (MP) conditions have been derived to locally relax the TVD constraints in the vicinity of extrema. We already demonstrated on various laminar test-cases [1, 2] that this scheme gives very accurate results at a very low-cost in terms of CPU time since it uses one-step integration, and is therefore very competitive compared to classical high-order methods of lines. The objective of this work is then to check the ability of the unlimited OS scheme and its limited version (OSMP) to accurately predict turbulent and shocked flows.

2 Equations and numerical scheme

We consider here the dimensionless compressible Navier-Stokes equations. For approximating the convective fluxes, the OS-7 scheme has been used that is 7^{th} order accurate in both time and space [1, 2]. In this study, by using the limited OSMP-7 scheme [1, 2], we review the influence of the Monotonicity-Preserving constraints on the characteristics of the turbulent flows. The diffusive terms of the Navier-Stokes equations are discretized by using a centered approximation. To study the influence of the order of accuracy of the

diffusive fluxes on the solution, second and fourth order accurate approximations are employed and compared on the test cases.

3 Numerical results

We evaluate separately the ability of the numerical schemes to compute turbulent flows with accuracy and to capture shock waves with robustness. Present results are evaluated on two canonical test-cases that have been considered in the International Workshop on High-Order CFD Method (HiOCFD workshop) to compare the CFD software performances [3]: namely, the three dimensional Taylor-Green vortex and the two dimensional steady shock wave laminar boundary layer interaction.
First, the well documented 3-D Taylor-Green vortex is considered at a Reynolds number $Re = 1600$ in a 3D periodic domain (Ω) of 2π non-dimensional side length [3, 4]. This problem allows us to evaluate the ability of the numerical procedure to compute transitional solutions in the basic framework of decaying Isotropic Homogeneous Turbulence (IHT).
Besides, the ability of the scheme to compute discontinuous solutions have been evaluated by performing the DNS of the steady shock wave laminar boundary layer interaction over a flat plate, experimentally and numerically studied by Degrez *et al.* [5].

3.1 Taylor Green vortex at Re=1600

The Taylor-Green vortex is a simple configuration allowing to simulate a turbulent energy cascade in the framework of isotropic homogeneous turbulence. A 3D periodic domain (Ω) of 2π non-dimensional side length is considered, in which a non dimensional initial flow field, which is an analytic solution of the Navier-Stokes equations, is given. This initial flow field consists in eight planar vortices. Nonlinear interactions between these initial vortices creates smaller and smaller scales until kinetic energy dissipation into heat following the so called Kolmogorov energy cascade.
The flow is completely characterized by the following set of non dimensional numbers values :

$$\begin{array}{l} M_0 = \frac{U_0}{c_0} = 0.1 \\ \gamma = 1.4 \\ Re_0 = \frac{\rho_0 U_0 L_0}{\mu_0} = 1600 \\ Pr_0 = \frac{\mu_0 Cp_0}{\lambda_0} = 0.71 \end{array} \tag{1}$$

where the reference variables (index 0) are characteristic scales of the flow at the initial time. U_0 is the greatest value of the flow speed in the domain. c_0 is the speed of sound in the domain, given by the uniform temperature T_0 in the domain. ρ_0 is the mean density. L_0 is the characteristic size of the domain. μ_0 and λ_0 are the initial dynamic viscosity and thermal conductivity of the fluid, given by the uniform temperature T_0. Cp_0 is the heat capacity at constant pressure of the fluid. The dynamic viscosity is assumed to be constant and it is evaluated using the value of the Reynols number.
Several uniform grids have been used to study grid convergence (namely, from 32^3 to 256^3).
The integral kinetic energy on the domain (Ω) is calculated at every time step during the simulation as follows:

$$E_k = \frac{1}{|\Omega|} \int_\Omega \rho \frac{\mathbf{v}.\mathbf{v}}{2} d\Omega, \tag{2}$$

where $\mathbf{v} = \{u_j\} \quad j \in [1, 3]$ is the velocity vector, ρ is the density and $|\Omega|$ is the volume of the domain (Ω).
We define the kinetic energy dissipation at every time step as:

$$\epsilon = -\frac{dE_k}{dt}. \tag{3}$$

We show that for a compressible flow and using the Stokes hypothesis, the kinetic energy dissipation can also be written as:

$$\epsilon = \frac{2\mu}{|\Omega|}\int_\Omega \mathbf{S}^d : \mathbf{S}^d d\Omega - \frac{1}{|\Omega|}\int_\Omega p\nabla.\mathbf{v}d\Omega, \tag{4}$$

where μ is the dynamic viscosity, $\mathbf{S}^d$ is the symmetric part of the strain rate tensor $\mathbf{S}$ with $S_{ij} = \frac{1}{2}(\frac{\partial u_i}{\partial x_j} + \frac{\partial u_j}{\partial x_i})$ where indexes $i, j \in [1, 3]$ are related to the space dimensions.
The enstrophy integral on the domain Ω is given by:

$$\varepsilon = \frac{1}{|\Omega|}\int_\Omega \rho\frac{\boldsymbol{\omega}.\boldsymbol{\omega}}{2}d\Omega, \tag{5}$$

where $\boldsymbol{\omega} = \nabla \times \mathbf{v}$.
For a compressible flow, the following approximate equality relating the kinetic energy dissipation and the enstropy stands:

$$\epsilon \approx 2\frac{\mu}{\rho_0}\varepsilon, \tag{6}$$

where ρ_0 is the mean initial density in the domain.
The time evolution of the kinetic energy, its dissipation and the enstrophy production in the domain are pivotal quantities representative of the energy cascade between turbulent scales and the turbulent vorticity production.

Results using the OS scheme Simulations where first performed using the unlimited 7^{th} order OS scheme and a second order spatial discretization for the diffusive terms. The simulations where performed at a constant CFL number value of 0.5. Figures 1, 2 and 3 show respectively the evolution of the kinetic energy, its dissipation and the enstrophy with respect to time for the different mesh size used (32^3, 64^3, 128^3, 256^3). The kinetic energy dissipation is computed using equation (3) by first order derivation of the evolution of the kinetic energy with respect to time. The enstrophy, is computed by equation (5). The vorticity components are approximated using 4^{th} order Pade scheme [6]. Results are compared to a reference solution obtained by a dealiased pseudo-spectral spatial discretization together with a three step Runge-Kutta scheme for the time integration, on a 512^3 grid [3].
We observe the convergence of the solution toward the reference solution when the mesh is refined. We see in figures 1 and 2 that the decrease of the kinetic energy in the domain can be splitted into two dinstinct zones. In the first zone between time 0 and time 9, the kinetic energy dissipation increases until it reaches a maximum value of almost 0.013 at time 9. This augmentation of kinetic energy dissipation is related to the transition to turbulence creating smaller and smaller structures through the Kolmogorov energy cascade until the energy dissipates at diffusive scales. The maximum of kinetic energy dissipation corresponds to an inflection point in the history of the kinetic energy. As far as no energy is injected in the domain (Ω) after the initial time, this maximum dissipation is followed by the second zone where the dissipation decreases as the flow relaxes.
The calculation on mesh 32^3 fails completely in evaluating the time and value of the maximum kinetic energy dissipation. In fact, the time of the maximum is close to 7 and the value of the maximum dissipation is largely under-estimated. It leads to an underestimation of the kinetic energy in the domain before time 10 and an overestimation after time 10. The history of the kinetic energy has the same qualitative behavior on the 64^3 but it is quantitatively closer to the reference value. The calculation on the 128^3 exhibits rather good approximation of the time of the maximum dissipation. Nevertheless, the maximum dissipation value is underestimated leading to a slightly overestimation of the kinetic energy after time of 10. The results using the 256^3 are almost converged as they are nearly the same as the reference results. In particular, we observe that the prediction of the time of maximum dissipation is correct and that the maximum dissipation value is only slightly under-estimated.
The history of the enstrophy exhibits the same qualitative behavior as the kinetic energy dissipation as they are approximately proportional (equation (6)). Again, the more we refine the mesh, the more the estimation of the enstrophy is close to the reference value. In particular, the time of maximum enstrophy and its value are not well predicted when using the 32^3 and 64^3 meshes. The prediction is correct for the time of maximum enstrophy when using the 256^3 mesh but its value is underestimated. Nevertheless the results obtained for

the history of the enstrophy compare well with the results of the HIOCFD workshop [7] [3].

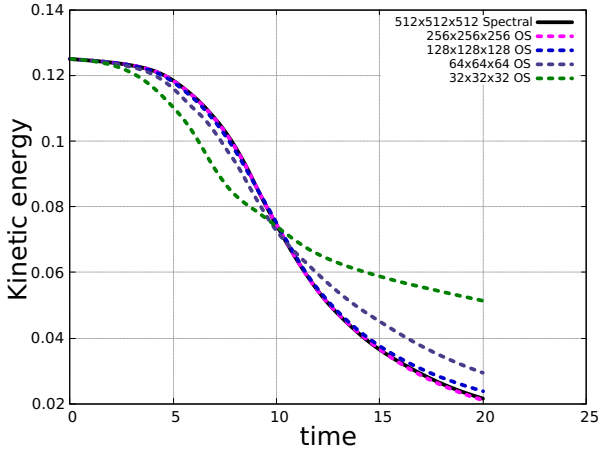

Figure 1: History of the kinetic energy obtained using the OS-7 scheme for different mesh sizes (32^3, 64^3, 128^3, 256^3). Present solutions are compared to the reference solution [3].

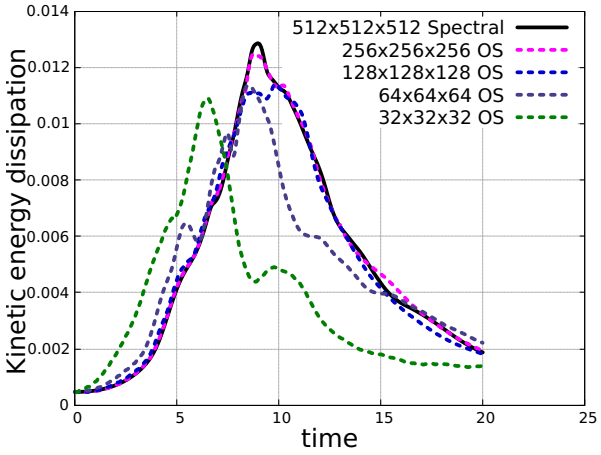

Figure 2: History of the kinetic energy dissipation obtained using the OS-7 scheme for different mesh sizes (32^3, 64^3, 128^3, 256^3). Present solutions are compared to the reference solution [3].

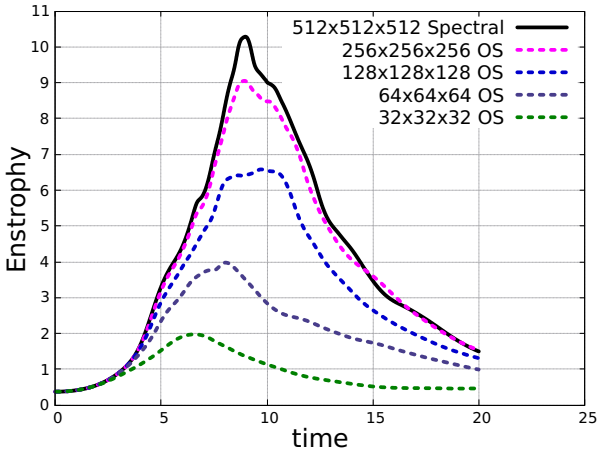

Figure 3: History of the enstrophy using the OS-7 scheme for different mesh sizes (32^3, 64^3, 128^3, 256^3). Present solutions are compared to the reference solution [3].

This grid convergence can be compared with results obtained using other numerical schemes whithin the HIOCFD workshop framework. Figures 4 and 5 show the grid convergence for the kinetic energy dissipation and the enstrophy dissipation. We define the L_∞ error of a quantity s with respect to the reference solution s^{ref} as:

$$Error_{L_\infty(t\in[0;10])} = max_{(t\in[0;10])} \mid s_k - s_k^{ref} \mid, \tag{7}$$

where s_k is the value of s at time $t^k = k.dt$ with dt the time step and $k \in \mathbb{N}$. The L_∞ errors for the kinetic energy dissipation and the enstrophy dissipation are plotted with respect to the length scale $h = \frac{1}{N}$ where N is the number of mesh points in each direction.
Results obtained using the OS-7 scheme compare well with one of the best results obtained by the HIOCFD workshop participants [7] [3]. The error obtained on the kinetic energy dissipation using the OS-7 scheme

is almost one order of magnitude smaller than the one obtained using the DG-4 scheme. The DG-4 scheme needs far more points than the OS-7 scheme to recover the same error levels. The same trend is obtained for the enstrophy dissipation error, even if the difference between the results obtained by the different schemes are not as huge as for the kinetic enery dissipation.

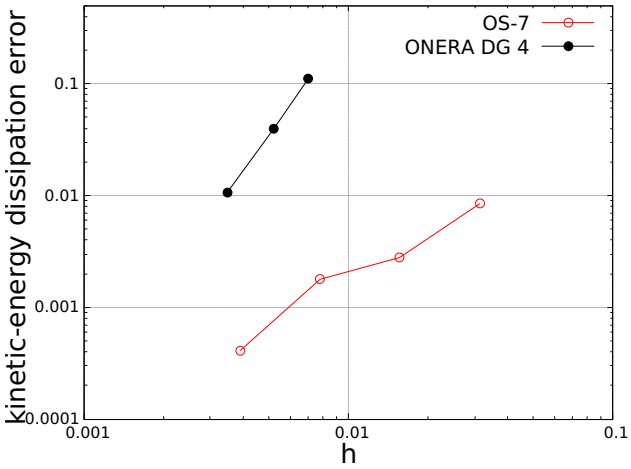

Figure 4: Grid convergence for the kinetic energy dissipation

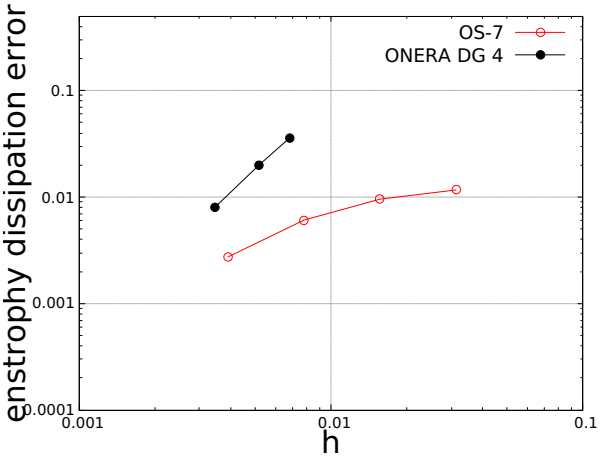

Figure 5: Grid convergence for the enstrophy dissipation

Effect of the MP constraint on the results The same simulations have also been performed using the shock capturing procedure. The figure 6 shows the kinetic energy with respect to the time using the OSMP-7 scheme for the different meshes used. The convergence toward the reference solution is still noticeable when using the shock capturing procedure. The results for the different meshes have the same qualitative behavior than the results using the OS scheme. The results using 32^3 and 64^3 do not predict the correct time of inflection point in the history of the kinetic energy. For those meshes, the kinetic energy is badly estimated during the entire time of the simulation. The kinetic energy is nearly correctly estimated when using the 128^3 mesh even if it is slightly overestimated after the time 15. The result using the 256^3 mesh is in good accordance with the reference result.

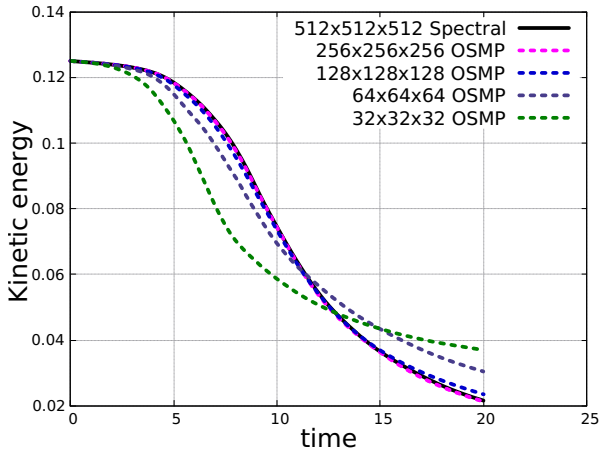

Figure 6: History of the kinetic energy obtained using the OSMP-7 scheme for different mesh size (32^3, 64^3, 128^3, 256^3). Present solutions are compared to the reference solution [3].

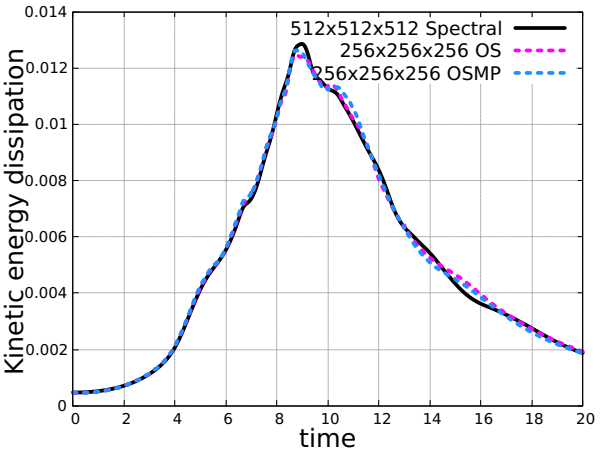

Figure 7: History of the kinetic energy dissipation obtained using the OS-7 and OSMP-7 schemes for the 256^3 mesh. Present solutions are compared to the reference solution [3].

The comparison between the kinetic energy dissipation evolution computed with and without the MP procedure on the 256^3 mesh is plotted on figure 7. For nearly converged computations, the results are almost the same, demonstrating that the MP constraint has a little influence when the solution is regular on the opposite of the TVD constraint that clips the extrema [1][2].
The L_∞ errors with respect to the reference obtained with and without the MP procedure are plotted on figure 8 and 9. The same level of errors are recovered in both cases. The use of the shock capturing procedure has a small influence on the computation of the enstrophy in the domain. The enstrophy is slightly underevaluated when using the OSMP-7 scheme (figure 9).
These results show that the MP constraint can efficiently be used to simulate regular flows on sufficiently refined meshes.

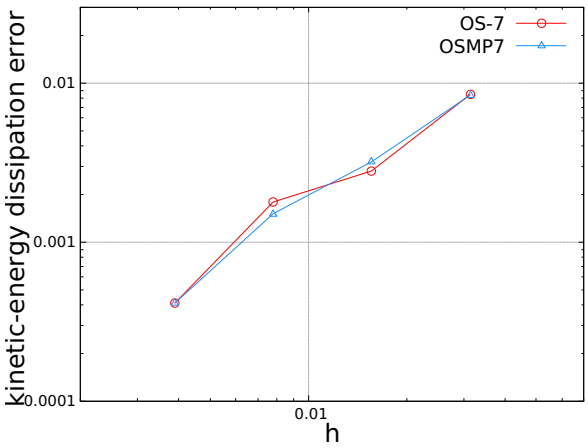

Figure 8: Grid convergence for the kinetic energy dissipation

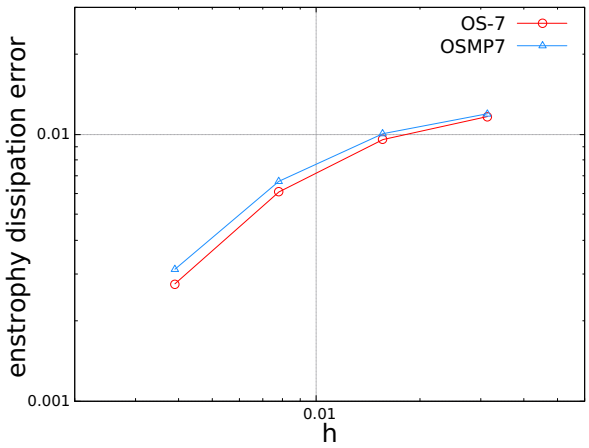

Figure 9: Grid convergence for the enstrophy dissipation

Influence of the order of accuracy for the discretization of the diffusive terms Simulations have also been performed using the OSMP-7 scheme coupled with a 4^{th} order centered finite difference approximation for the diffusive fluxes as far as the high order approximation might have an influence on the dissipation process occuring at small scales. The 4^{th} order approximation have been checked on a manufactured solution to review the accuracy. 4^{th} order accurate solution is clearly obtained (not shown here). The history of the kinetic energy is plotted on figure 10. The results are qualitatively the same than those using a second order discretization for the diffusive fluxes. In particular, the simulation on the 256^3 mesh is in good agreement with the reference results. The history of the kinetic energy dissipation is compared here after with the results obtained using a 2^{nd} order centered finite difference approximation for the diffusive fluxes. This comparison suggests that the use of an order higher than second order for the diffusive fluxes have almost no influence on the results for such a converged simulation at relatively high Reynolds number.

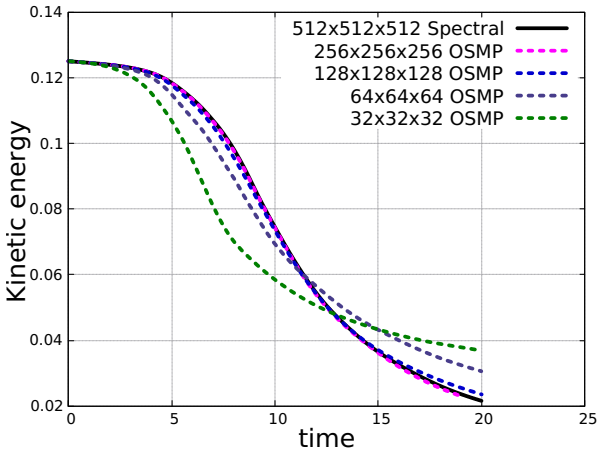

Figure 10: History of the kinetic energy obtained using the OSMP-7 scheme and a 4^{th} order discretization for the diffusive fluxes on different meshes of (32^3, 64^3, 128^3, 256^3) size. Present solutions are compared to the reference solution [3].

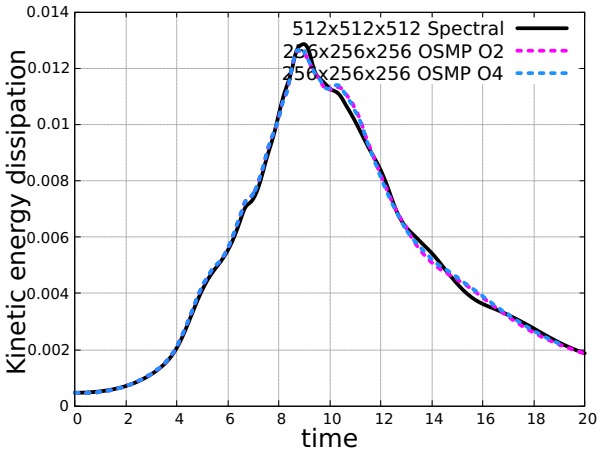

Figure 11: History of the kinetic energy dissipation obtained using the OSMP-7 on the 256^3 mesh. Results using a second 2^{nd} and a 4^{th} order discretization for the diffusive fluxes are compared. Present solutions are compared to the reference solution [3].

The L_∞ error with respect to the reference obtained using 2^{nd} or 4^{th} order discretization of the diffusive terms is plotted on figure 12 with respect to the mesh size. The results are almost identical for the 32^3, the 64^3 and the 128^3. The error is slightly lowered when using the 4^{th} order discretization of the diffusive terms on the 256^3 mesh. As the diffusion processe is occuring at small scale, it is not surprising that discrepancies are found for fine meshes able to evaluate the role of the diffusion at small scale. The L_∞ errors are nearly the same in both cases demonstrating that using higher order than 2 for the diffusive fluxes is not mandatory for such high Reynolds number simulations.

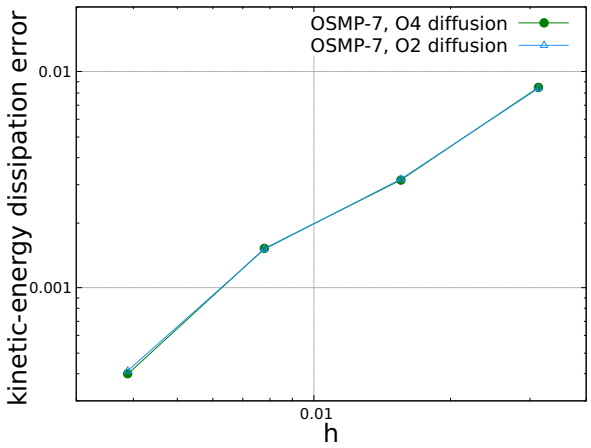

Figure 12: Grid convergence for the kinetic energy dissipation.

3.2 Laminar shock boundary layer interaction

We consider the interaction between an incident oblique shock wave impigning a laminar boundary layer developing over a flat plate. The interaction produces a separation of the flow and a subsequent recirculation bubble. This flow has been experimentally and numerically studied in [5].

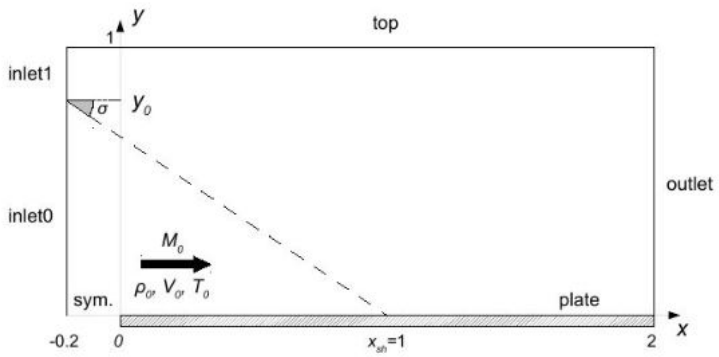

Figure 13: Computational domain with non-dimensional dimensions and boundary conditions. The dashed line represents the inviscid incident shock position [8].

Sketch of the computational domain is given figure 13. A uniform flow is imposed at the inlet using non reflecting characteristic based inlet conditions [9]. At a height of y_0, the Rankine-Hugoniot relationships are imposed, so that a shock of angle $\sigma = 38.5°$ is created in the domain that impinges the wall at $x_{sh} = 1$. No-slip and adiabatic wall conditions are imposed for $y = 0$ and $x > 0$ whereas symmetric boundary condition is imposed in front of the leading edge of the flat plate. Outlet time dependent boundary conditions are imposed at the top and at the outlet boundaries regions [9].
The flow in the region inlet 0 ($y < y_0$) is prescribed by using the non dimensionalized numbers that completely characterize the flow:

$$\begin{aligned} M_0 &= \frac{U_0}{c_0} = 2.15, \\ Re_0 &= \frac{\rho_0 U_0 x_{sh}}{\mu_0(T_0)} = 10^5, \\ Pr_0 &= \frac{\mu_0 Cp_0}{\lambda_0(T_0)} = 0.71, \\ \gamma &= 1.4, \end{aligned} \tag{8}$$

where c_0 is the speed of sound given by the uniform temperature T_0 imposed at the boundary region inlet 0. ρ_0 is the uniform density imposed at the boundary region inlet 0. x_{sh} is the abscissa at which the shock should impinge the flat plate in nonviscous flow ; it is taken as the reference length scale. μ_0 and λ_0 are the dynamic viscosity and thermal conductivity of the fluid, given by the uniform temperature T_0 at the inlet. The evolution of the dynamic viscosity and the thermal conductivity with the temperature is given by the Sutherland's law. Cp_0 is the heat capacity at constant pressure of the fluid injected through the region inlet 0.
An example of the mesh employed for the simulation is given in figure 14. The domain is discretized using a cartesian mesh with non uniform spacing in both x and y directions. In the longitudinal direction, the mesh is refined in the vicinity of the flat plate leading edge and in the vicinity of the shock wave impact abscissa x_{sh}. In the vertical direction, the mesh is progressively tightened close to the wall using a hyperbolic tangent law to obtain a minimum grid spacing at $y = 0$. The minimum grid spacing is $\Delta y_{min} = 10^{-4}$.

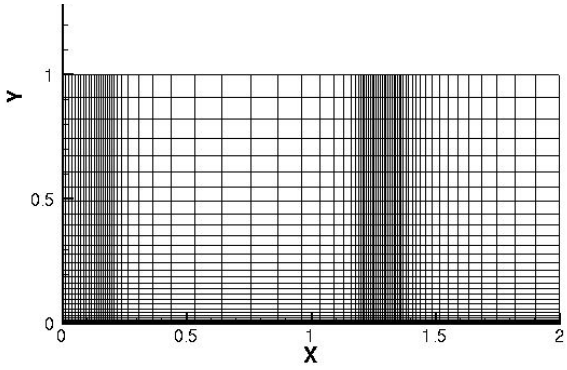

Figure 14: Mesh used for the calculation.

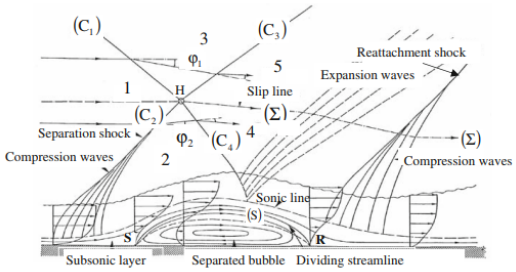

Figure 15: Schematic of the flow field [10].

Sketch of the flow is given figure 15. The presence of the impinging shock wave imposes a sharp adverse pressure gradient to the flow. In the configuration presently studied, the adverse pressure gradient is strong enough to enable a separation of the boundary layer (point S on figure 15) that reattaches further downstream (point R on figure 15) forming a separation bubble. A sonic line appears at the edge of the bubble (noted (S) on figure 15). This kind of shock wave boundary layer interaction is called strong interaction, contrary to a weak shock wave boundary layer interaction where no separation occurs. The flow being subsonic under the sonic line (S), the pressure rise due to the incident shock (C_1) is felt upstream of where the incident shock would have impacted the wall, explaining the upstream position of the separation point. The presence of the recirculation bubble induces compression waves that converge to form the reflected shock (C2). The incident shock (C1) is transmitted as (C4) through the separation shock (C2) and is reflected as expansion waves. At the reattachement point (R), the deviation of the supersonic flow due to the wall leads to compression waves that also coalesce to form the so called reattachement shock. In this configuration, the viscosity at play in the boundary layer leads to a complete reorganisation of the flow even in the outer region where a different system of shock waves is created, with respect to the inviscid shock wave reflexion on a wall.

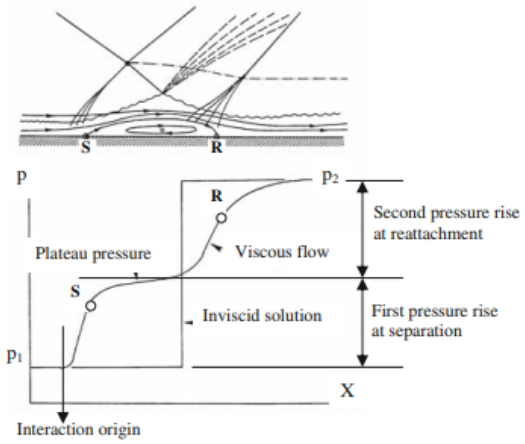

Figure 16: Pressure at the wall for a strong shock wave boundary layer interaction [10]

Such a strong interaction is characterized by a characteristic wall pressure distribution as shown on figure 16 where the wall pressure distribution for a strong shock wave boundary layer interaction is compared with the distribution for an inviscid shock wave reflection. The first part of the interaction consists in a steep rise of the pressure associated with the separation followed by a plateau like of pressure characteristic of separated flows. The second part of the interaction consists in a second wall pressure rise associated with the reattachment process, leading to the same pressure as in the inviscid case. The wall pressure distribution is then an important quantity to assess the accuracy of the simulations.
The extent of the recirculation bubble is driven by the intensity of the incident shock wave, let say the pressure ratio from each side of the shock, and by the incoming boundary layer velocity profile. Indeed, the stronger the shock, the stronger the adverse pressure gradient leading to the separation of the boundary layer. Furthermore, the sharper the boundary layer velocity profile is, the more the boundary layer resists to separation caused by the adverse gradient pressure. For instance, a laminar boundary layer is more prone to separation than a turbulent one when subjected to a steep adverse pressure gradient. The separation bubble extent then characterizes the interaction studied. The skin friction coefficient C_f, as defined in equation (9), is then an important quantity to calculate, as it allows to determine the position of the separation (where C_f becomes negative) and reattachement points (where C_f becomes again positive). The skin friction coefficient is defined by the following equation :

$$C_f = \frac{\tau_w}{\frac{1}{2}\rho_\infty U_\infty^2}, \tag{9}$$

where $\tau_w = \mu \frac{\partial u}{\partial y}|_{y=0}$ is the shear stress at the wall.

As previously described, due to the strong shock wave boundary layer interaction studied here, a complex system of shock waves, compression and expansion waves is formed in the supersonic part of the flow. The accuracy of the calculation in this part of the flow depends greatly on the ability of the numerical scheme to capture the discontinuities (shock waves) without spoiling the accuraty of the solution in the vicinity of the discontinuity. In the following, we evaluate the efficiency of the shock capturing procedure evaluating the pressure distribution in the supersonic part of the flow at a height of y=0.1.

Convergence study Figure 17, 18 and 19 show respectively the wall pressure distribution, the skin friction coefficient and the pressure distribution at $y = 0.1$ for different mesh size obtained using the OSMP-7 scheme and a 2^{nd} order centered finite difference approximation for the diffusive fluxes. The different mesh sizes considered are 80×40, 200×100, 280×140, 360×180 and 480×240. The use of the limited version of the scheme OSMP-7 is first favoured as far as shocked flow is considered here.
The wall pressure distribution estimated by the numerical scheme is in accordance with the theoretical considerations previously reminded. Indeed we see on figure 17 that for each mesh used, the qualitative

behavior of the wall pressure distribution is correct, consisting in two steep rises of the wall pressure separated by a plateau like of pressure. The wall pressure values before and after the interaction are the same for each mesh size used. Nevertheless, the wall pressure distribution inside the interaction is different for every mesh size and we observe a convergence towards a converged solution. The more the mesh is refined, the more the first pressure increase begins earlier and the second pressure rise ends later. The value and the extent of the plateau like of pressure is nearly the same for every meshes except for the 80×40 where the value of the pressure is clearly under-estimated in the plateau. Moreover, for the 80×40 mesh, the second rise of pressure is largely sharper than for the other meshes. As for the wall pressure distribution, we observe a grid convergence towards a converged solution for the skin friction coefficient distribution shown on figure 18. We observe that, the thinner the mesh, the smaller the abscissa of the separation point and the bigger the abscissa of the reattachment point exept for the 80×40 mesh that completely fails in estimating the skin friction distribution. The pressure distribution at $y = 0.1$ is shown on figure 19 for the different meshes. For this vertical coordinate, the pressure distribution is composed of a first almost discontinuous compression corresponding to the incident shock (C1) followed by a continuous compression corresponding to the reflected compression waves (C2) that don't coalesce to form a shock in our test case configuration. This continuous compression is followed by a sharp decrease of the pressure corresponding to the expanssion waves. It is followed by a continuous compression due to the compression waves related to the reattachement of the boundary layer. We see that the mesh refinement influences the ability to compute sharp solutions. Indeed, we clearly see that non refined meshes of 80×40 and 200×100 tend to spread the sharp evolutions of the pressure namely the shock wave and the expansion waves. As for the wall pressure distribution and the skin friction coefficient, we observe a convergence of the results towards a converged solution. For the three quantities considered in figures 17, 18 and 19, only negligible differences exist between the results on the 360×180 mesh and the 480×240 mesh. Therefore we conserve the solutions on the 480×240 mesh to be the converged ones in the following.

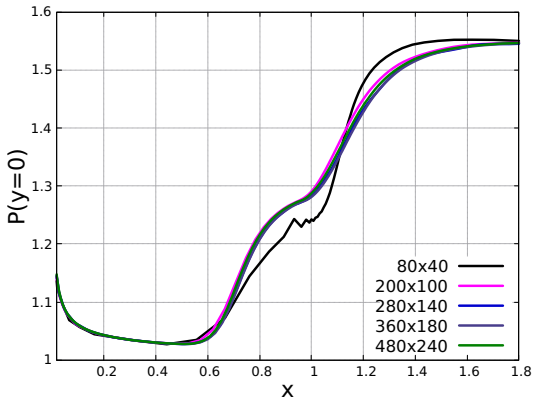

Figure 17: Wall pressure distribution using the OSMP-7 scheme and a 2^{nd} order centered finite difference approximation for different mesh size

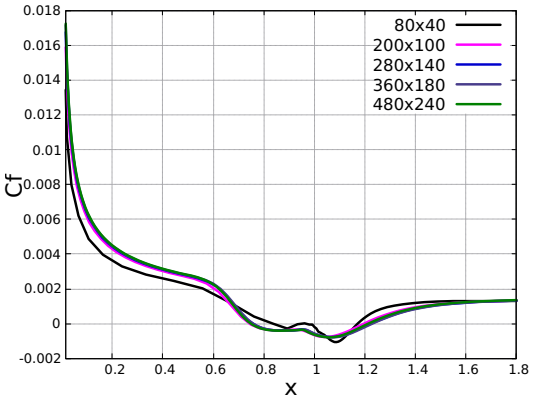

Figure 18: Skin friction coefficient distribution using the OSMP-7 scheme and a 2^{nd} order centered finite difference approximation for different mesh size

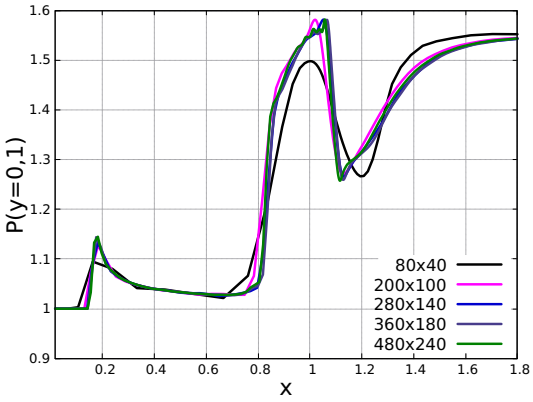

Figure 19: Pressure distribution at y=0.1 using the OSMP-7 scheme and a 2^{nd} order centered finite difference approximation for different mesh size

Effect of the MP constraints on the results The effect of using the OSMP-7 instead of the OS-7 scheme is highlighted on figures 20, 21 and 22 on which the results obtained using the OS-7 and OSMP-7 are plotted for the 480×240 mesh. As expected, the figure 22 highlights that the use of the OS-7 scheme leads to spurious oscillations in the vicinity of the discontinuities (shock waves). These oscillations are almost cancelled when the shock capturing procedure is activated, namely when the OSMP-7 scheme is used. No noticeable differences are observed for the wall pressure distribution between the results obtained using the OS-7 and the OSMP-7 schemes. Thus, the spurious pressure oscillations produced around the shock wave don't influence the wall pressure distribution. On the contrary, the skin friction calculated with the OS-7 scheme differs slightly from the skin friction coefficient calculated using the OSMP-7 scheme in the recirculation zone, where oscillations are observed for the results using the unlimited scheme. It shows that the spurious oscillations created in the viscinity of the discontinuities influence the solution in the entire domain.

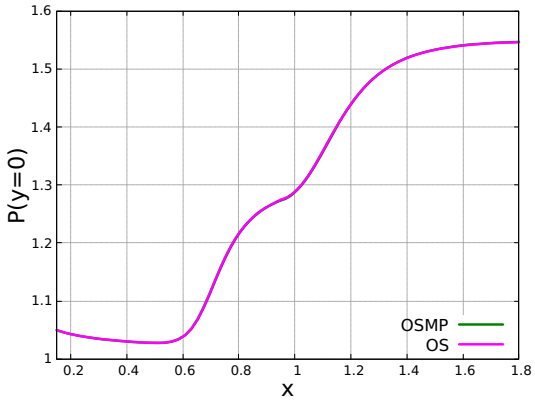

Figure 20: Wall pressure distribution for the 480×240 mesh

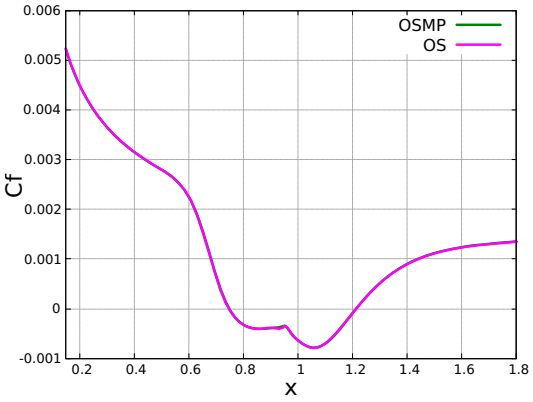

Figure 21: Skin friction coefficient distribution for the 480×240 mesh

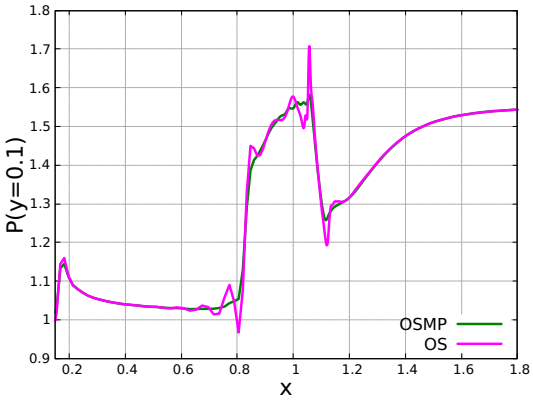

Figure 22: Pressure distribution at y=0.1 for the 480×240 mesh

Results comparison with other numerical and experimental results Previous results are compared with either experimental or numerical results. The experimental results come from Degrez *et al.* [5] who designed the present test case. Degrez *et al.* also provide numerical results. Two other numerical results have also been selected to compare with : the DNS of Gross and Fasel using a 9^{th} accurate WENO method based on the Van Leer (VL) flux vector splitting scheme [11] and the DNS of Blanchard and Renac performed in the framework of the HIOCFD workshop using a 6^{th} order discontinuous galerkin scheme [8].
The comparison of the wall pressure distributions is plotted on figure 23. It is noteworthy that the pressure levels before and after the interaction are the same for every results. Moreover, the results using the OSMP-7 scheme match nearly perfectly with the results obtained by Blanchard and Renac, even in the interaction zone. As explained previously, the interaction zone begins as a sharp rise of pressure. The beginning of the interaction zone is not the same for the numerical and experimental results of Degrez *et al.*. The interaction begins earlier for the numerical result. The beginning of the first rise of pressure of all the other results are between the numerical and experimental values of Degrez *et al.*. The same observation stands for the end of the interaction, that is predicted earlier for the numerical result with respect to the experimental result of Degrez *et al.*. The first rise of pressure predicted by the OSMP-7 and by the DNS of Blanchard and Renac is sharper than the ones calculated by the other autors. Consequently, the plateau like of pressure begins earlier for these two results with respect to the other results. The plateau like of pressure have nearly the same extent for all the results, then, the second rise of pressure, due to the reattachement, has more or less the same qualitative behavior for all the results except for the numerical result of Degrez *et al.* where the calculated recompression at the wall is faster.
The skin friction coefficient obtained are compared on figure 24. Degrez *et al.* only provided the separation and reattachement points experimentally mesured. Again, we observe that the result obtained using the OSMP-7 scheme is in good accordance with the result of Blanchard and Renac. In particular, the separation and reattachement points predicted are the almost the same. The skin friction distribution provided by Gross and Fasel is in good accordance with the one obtained using the OSMP-7 before the interaction begins. Nevertheless, the beginning of the interaction is located later in the Gross and Fasel's result leading to a separation point located at an abscissa bigger than the one predicted by the OSMP-7 and by the DNS of Blanchard and Renac. Moreover, the reattachement point abscissa calculated by Gross and Fasel is greater than the one predicted in our study. The numerical computation of the skin friction provided by Degrez *et al.* does not match the other results before the beginning of the interaction. The separation point predicted by Degrez *et al.* is in accordance with the one predicted by Gross and Fasel. Nevertheless, the reattachement point calculated by Degrez *et al.* is close to the one computed in our study. The experimental mesurement of the separation point is in between the separation point calculated in our study and the separation point given by Gross and Fasel. The experimental reattachement point is the same than the one provided by Gross and Fasel. The pressure distribution at $y = 0.1$ obtained in our study is compared with the distribution provided by Blanchard and Renac on figure 25. No shock capturing constraint is used in the DNS of Blanchard and Renac explaining the spurious oscillations in the vicinity of the discontinuities. The slopes of the pressure

variations and the locations of the shock wave, the expansion waves and the reattachement recompression are the same in both simulations.

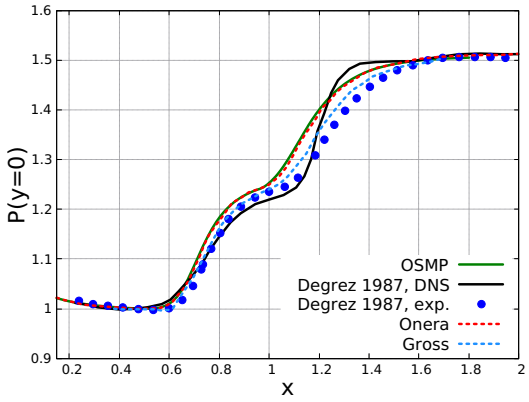

Figure 23: Wall pressure distribution for different schemes

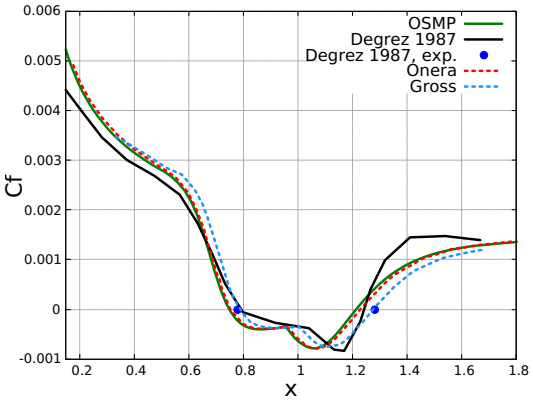

Figure 24: Skin friction coefficient distribution for different schemes

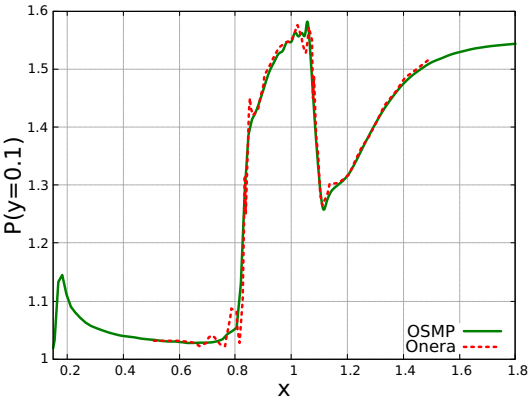

Figure 25: Pressure distribution at y=0.1 for different schemes

Influence of the order of accuracy for the discretization of the diffusive terms The comparison of the results obtained using the OSMP-7 scheme coupled with a 4^{th} order centered finite difference approximation for the diffusive fluxes are compared with those using a 2^{nd} order centered finite difference approximation. No differences are noticeable between the results, even for quantities calculated close to the wall where viscosity plays a dominant role. It shows that a 2^{nd} order centered finite difference approximation for the diffusive fluxes is sufficient to simulate flows at such high Reynolds number.

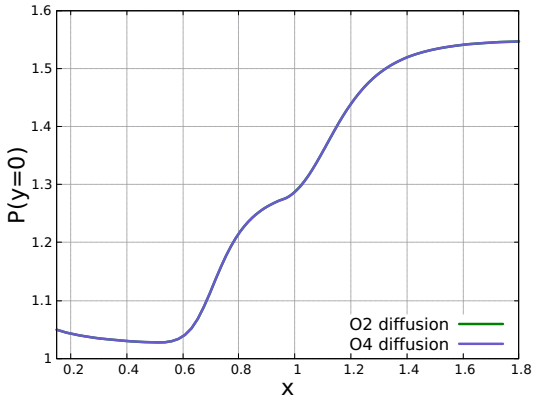

Figure 26: Wall pressure distribution for the 480×240 mesh calculated using either 2^{nd} order or 4^{th} order approximation for the diffusive fluxes.

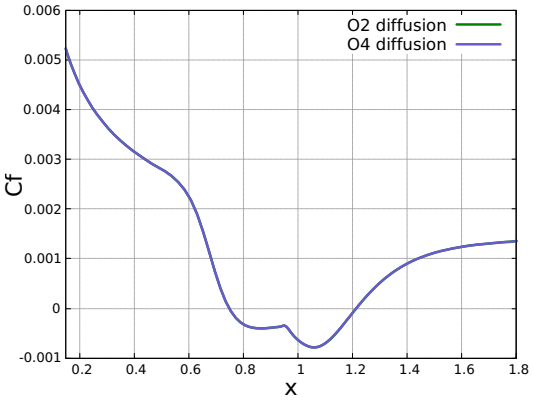

Figure 27: Skin friction coefficient distribution for the 480×240 mesh calculated using either 2^{nd} order or 4^{th} order approximation for the diffusive fluxes.

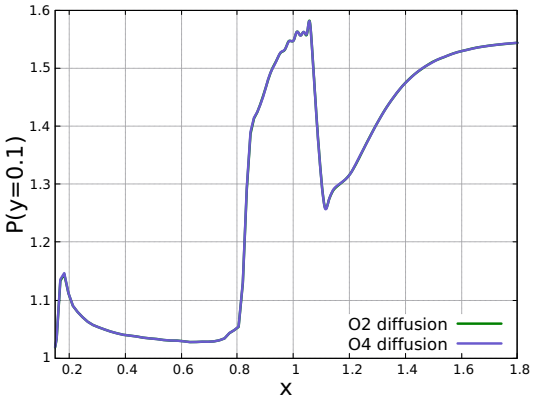

Figure 28: Pressure distribution at y=0.1 for the 480×240 mesh calculated using either 2^{nd} order or 4^{th} order approximation for the diffusive fluxes.

4 Conclusion

The ability of the OSMP-7 scheme to accurately compute high Reynolds compressible flows has been assessed for two well documented test-cases coming from the HiOCFD workshop: the Taylor-Green vortex problem and the laminar shock-wave boundary layer interaction. Results demonstrate the correct accuracy of the OSMP-7 scheme to predict turbulent features and the great efficiency of the MP procedure to capture discontinuity without spoiling the solutions. Moreover, the order of accuracy higher than 2 for approximating the diffusive fluxes seems to have negligible influence on the solution for such relatively high Reynolds numbers. Following these results, it is with confidence that we can undertake the simulation of shock wave-turbulent boundary layer interaction.

References

[1] V. Daru and C. Tenaud. High Order One-step Monotonicity-Preserving Schemes for Unsteady Compressible flow Calculations. *Journal of Computational Physics*, 193(2):563–594, 2004.

[2] V. Daru and C. Tenaud. Numerical simulation of the viscous shock tube problem by using a high resolution monotonicity-preserving scheme. *Computers & Fluids*, 38:664–676, 2009.

[3] Z.J. Wang et al. High-Order CFD Methods: Current Status and Perspective. *International Journal For Numerical Methods In Fluids*, 72(8):811–845, 2013.

[4] M. Brachet et al. Small-scale structure of the Taylor-Green vortex. *Journal of fluid mechanics*, 130(23):411–452, 2006.

[5] G. Degrez et al. The interaction of an oblique shock wave with a laminar boundary layer revisited. An experimental and numerical study. *Journal of fluid mechanics*, 177(13):247–263, 1987.

[6] S. K. Lele. Compact finite difference schemes with spectral-like resolution. *Journal of Computational Physics*, 103(1):16–42, 1992.

[7] HiOCFD4 Committee. HiOCFD4 web site. [https://how4.cenaero.be], 2016.

[8] R. Blanchard and F. Renac. Baseline test case summaries. Case BL2: Shock Wave / Laminar Boundary Layer Interaction. [https://how4.cenaero.be], 2016.

[9] K.W. Thompson. Time Dependent Boundary Conditions for Hyperbolic Systems. *Journal of computational physics*, 68(1):1–24, 1987.

[10] J. Delery. Some physical aspects of shock wave/boundary layer interactions. *Shock Waves*, 19(6):453–468, 2009.

[11] A. Gross and H. Fasel. Numerical Investigation of Shock Boundary-Layer Interactions. *54th AIAA Aerospace Sciences Meeting,San Diego, California, USA*, 2016.